

Unraveling and Mapping the Mechanisms for Near-surface Microstructure Evolution in CuNi Alloys under Sliding

Stefan J. Eder,^{*,†,‡} Manel Rodríguez Ripoll,[†] Ulrike Cihak-Bayr,[†] Daniele Dini,[¶]
and Carsten Gachot^{†,‡}

[†]*AC2T research GmbH, Viktor-Kaplan-Straße 2/C, 2700 Wiener Neustadt, Austria*

[‡]*Institute of Engineering Design and Product Development, TU Wien, Getreidemarkt 9,
1060 Vienna, Austria*

[¶]*Department of Mechanical Engineering, Imperial College London, South Kensington
Campus, Exhibition Road, London SW7 2AZ, UK*

E-mail: stefan.j.eder@tuwien.ac.at

Phone: +43 (0)2622 81600 161. Fax: +43 (0)2622 81600 99

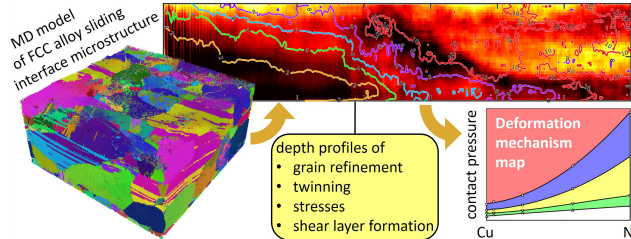
This document is the Accepted Manuscript version of a Published Work that appeared in final form in *ACS Applied Materials & Interfaces*, copyright © American Chemical Society after peer review and technical editing by the publisher. The version of record is available here. The Supporting Information is available here.

Abstract

The origin of friction and wear in polycrystalline materials is intimately connected with their microstructural response to interfacial stresses. Although many mechanisms that govern microstructure evolution in sliding contacts are generally understood, it is still a challenge to ascertain which mechanisms matter under what conditions, which limits the development of tailor-made microstructures for reducing friction and wear. Here, we shed light on the circumstances that promote plastic deformation and surface damage by studying several FCC CuNi alloys subjected to sliding with molecular dynamics simulations featuring tens of millions of atoms. By analyzing the depth- and time-dependent evolution of the grain size, twinning, shear, and the stresses in the aggregate, we derive a deformation mechanism map for CuNi alloys. We verify the

predictions of this map against focused ion beam images of the near-surface regions of CuNi alloys that were experimentally subjected to similar loading conditions. Our results may serve as a tool for finding optimum material compositions within a specified operating range.

Keywords: deformation mechanism map, microstructure evolution, fcc alloys, sliding contact, large-scale molecular dynamics



Introduction

When two materials are pressed together and slide against each other, in the greatest majority of instances there are inelastic changes induced by this interaction. Yet, scientists are still struggling to rank the governing mechanisms responsible for the behavior and evolution of sliding interfaces, which in turn strongly influence friction and wear, by their relevance under a given set of operating conditions. This is particularly important for polycrystalline metallic materials; despite great effort and progress recently made to elucidate the microstructural evolution in metallic sliding contacts,^{1,2} there are many questions that remain unanswered. One of these key questions is the subject of our investigation: can we explain how sliding affects microstructural evolution in relevant metallic alloys?

Numerous microstructural processes linked to severe deformation and various testing conditions have been observed and explained in the past; these include, e.g., dislocation mediated grain refinement^{3,4} and grain boundary sliding.^{5,6} Looking at sliding processes in dry contacts, where frictional energy is mainly dissipated by plastic deformation and material flow, they are usually accompanied by high strain rates, large strain gradients, possibly intermix-

ing of the contacting materials,^{7,8} recovery, and (both static and dynamic) recrystallization.^{9,10} This comes along with the formation of stable and metastable microstructural changes observed in metallic materials^{11,12} and the formation of flow-like patterns resembling fluid flow, which can be identified in particular if mixing of materials takes place and have been compared to Kelvin-Helmholtz shear instabilities or vortex instabilities in the literature.¹³⁻¹⁵

On the one hand, it could be shown that grain growth follows nanocrystalline grains in a surface subjected to sliding;^{16,17} on the other hand grain refinement was detected when loading annealed coarse-grained materials.^{18,19} Depending on load, sliding speed, temperature, or initial grain size, new microstructures may develop beneath the sliding contact, effectively reducing friction and wear. The key question to address is which regimes and experimental conditions promote the occurrence of a particular microstructure exhibiting low or high friction. Argibay *et al.* linked microstructural evolution to macro-scale friction behavior in metals.²⁰ They identified a low-friction regime that was strongly connected to ultra-nanocrystalline surface layers with shear accommodation by grain boundary sliding, whereas a high-friction regime was dominated by dislocation-mediated plastic-

ity. Based upon this, they created generalized dimensionless friction maps, clearly marking the transition between grain boundary sliding and dislocation-mediated plasticity as a function of reduced time and stress. The respective deformation limits in these friction maps are strongly influenced by the stacking fault energy (SFE) and thus twinning.^{21,22} Experimental reports have shown that a higher SFE usually results in changes in the wear resistance, where recent work suggests an increase,²³ while some earlier works reported a decrease^{24,25} or found no definite trend.²⁶ Another important aspect to consider is the atomistic origin and the complexity of dislocation and grain boundary behavior as well as their interactions when subjected to high strain rates and localized energy inputs.^{27,28} Yet, the understanding of the microstructural processes in sliding contacts of FCC metals that considers all important aspects associated with the evolution of the surface and subsurface layers is still lacking.

In our research, we have analyzed and compared the results of dozens of large-scale polycrystalline molecular dynamics (MD) simulations (spanning a considerable parameter space over load, composition, and time) to unravel and map fundamental mechanisms for near-surface microstructural evolution in CuNi alloys under sliding at constant strain rate and temperature. CuNi alloys have numerous applications such as in shipbuilding, offshore oil production, power plants,²⁹ electrical sliding contacts,³⁰ and they are used in a similar fashion as CuAl coatings in tribological interfaces of jet engine compressors.³¹ MD simulations have become increasingly valuable for providing insight into microstructural changes in polycrystalline materials during sliding.^{2,32–34} CuNi is an ideal alloy system in which both constituents form an isomorphous system without phase precipitation, where the SFE varies by a factor of three between pure Cu and Ni, and a fast and reliable force field exists that allows a treatment using MD.³⁵ The results for various Ni contents reveal the time de-

velopment of a load and composition dependent shear layer (also discussed in terms of a “shear-induced flow layer”³⁶ or a “plastic strain-rate profile”³⁷ in the literature) as well as changes in stress and twin boundaries. Our systematic investigation of single-phase FCC alloy deformation allows us to derive a deformation mechanism map as a function of load and composition, assigning grain refinement, twinning, lattice rotation, and shear layer formation to said parameter combinations. There are many ways of potentially presenting and discussing our findings, as for example using the peak deviatoric stresses occurring within the system to quantify the effect of the stress tensor on plastic deformations; however, here we plot the quantities of interest over the normal pressure, which can be directly related to the applied load as an external independent variable controlled at design level. Our fundamental findings have a good prospect of being transferred to other FCC metals and alloy systems and thus driving the design of future advanced materials and coatings with superior properties in sliding contacts.

Results and Discussion

Computational micrographs

In our simulations, a rough rigid counterbody is pressed at several constant normal pressures σ_z against a polycrystalline FCC microstructure characterized by an average grain size of 40 nm, which in this work will be referred to as “coarse”, see Fig. 1a and b. The initial grain size places the microstructure solidly within the Hall-Petch regime;^{2,38} however, the space available for the formation of dislocations is limited.³⁹ The two surfaces slide against each other for up to 7 ns at a relative velocity of $v_x = 80$ m/s, chosen for computational feasibility.⁴⁰ Apart from an increased propensity towards twinning due to this high strain rate, we do not expect any behavior that differs fundamentally from

that seen at lower sliding speeds, especially as the system is prevented from artificial overheating by use of an electron-phonon coupling based thermostatting scheme.⁴¹ All investigated CuNi alloys (abbreviated CuNi X , where X is the atomic percentage of Ni) are random solid solutions that share the same grain structure and orientations.

The microstructural evolution of the polycrystalline aggregate reveals the presence of the following deformation mechanisms. Since FCC materials preferentially take up plastic strain by twinning at high strain rates,²¹ this mechanism dominates in our simulations because of the high sliding velocity, see Fig. 1c–f. Given that the SFE defines the surface energy of the twins, the twin density should be lower for alloys with higher SFE. This is indeed captured by our simulations, where we observe lower twin boundary fractions at higher Ni contents under otherwise identical loading conditions. Additionally, we observe that deformation is accommodated by partial lattice rotation, shown in Fig. 1d and e. During the initial stages when most of the grains are comparatively large, partial lattice rotation dominates. As further sliding promotes rotation, this results in the subsequent formation of new grain boundaries.

The refined grains take up further plastic strain by twinning, leading to even narrower twins, and in addition they accommodate the imparted deformation by lattice rotation. As a result, hardly any of the surface grains retain the orientations they had upon formation. As soon as grain refinement spreads over the layer of grains that covers most of the sample surface, the process speeds up considerably, since lattice rotation is promoted as the grains become smaller, see Fig. 1e.

The re-orientation of the refined grains, many of which are in the 10 nm range, by grain boundary sliding ultimately results in the formation of a shear layer. Simultaneously, new twins form with a strong tendency to be parallel to the sliding interface, as shown in Fig. 1f. Within the growing shear layer, further rotation leads to co-

alescence of grains, and the newly formed large grains deform along the sliding direction, leading to strongly elongated grains, see Fig. 1g. This behavior is also influenced by the limited depth (40 nm) of the sample, which introduces features typical of confinement that are often observed in soft metal coatings deposited on hard substrates and rubbing against hard materials,^{14,36} as well as in confined viscous fluids subjected to high pressures and shear rates.⁴³

Deformation mechanism map

We have distilled the results of approximately 4 million core hours worth of MD simulations into a single map of deformation mechanisms for CuNi alloys as a function of composition and contact pressure, see Fig. 2a. The full details of how we simplified the large amount of raw data to produce the map will be given in the next section. In the following, we will walk the reader through this map, explaining the individual regions and justifying the boundaries between them via comparison with some experimental data. We emphasize here that all of the round white data points in Fig. 2a follow from our simulation results at constant temperature and strain rate, using only a few assumptions that will be discussed in more detail in section . Furthermore, all time dependent aspects of the microstructural development have already been eliminated from the data that went into producing this map, i.e., only systems that had already reached equilibrium were considered. The data points then yield the shown regime boundaries via polynomial fitting (the parameters for which are listed in Fig. 2). The map is surrounded by representative snapshots of simulations and focused ion beam (FIB) cross-sections of experimental samples with compositions and loading conditions that follow within the map (cf. the annotations in the individual panels). The solid black data points mark where the surrounding examples are located within the map. Protective Pt layers were deposited

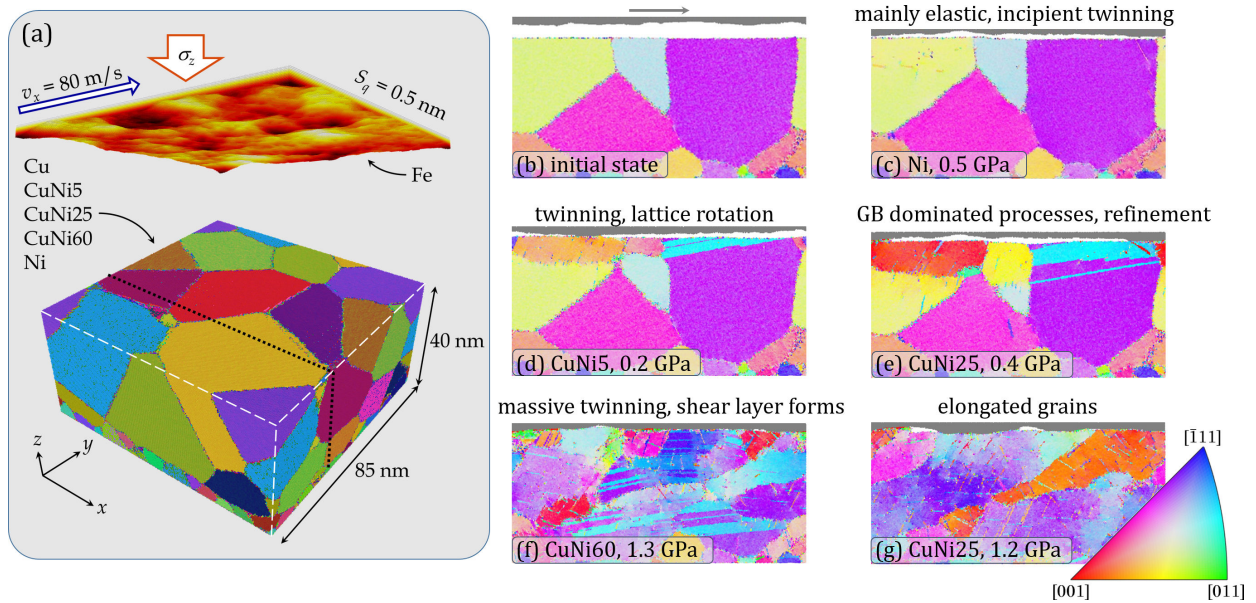


Figure 1: System overview and observed microstructural evolution. (a) Exploded perspective 3D-sketch of the MD system used for all simulations. The base body is colored according to grain orientation in Rodrigues space,⁴² whereas the sliding counterbody is colored according to surface topography with an RMS surface roughness of 0.5 nm. Right: Representative cross-sections before (b) and after sliding (c–g), located at the dotted black line in (a), providing snapshots of the phenomena discussed in this work. Colored according to grain orientation (EBSD-IPF color standard, see legend). The X in CuNi X denotes the atomic percentage of Ni.

on the experimental samples where the focus lay on observing small features located close to the tribological interface, while in the more severely deformed samples we dispensed with a Pt layer in favor of a clear view of the sample surface. Our comparison is aimed at showing that the phenomena captured by the atomistic simulations qualitatively reproduce the deformation mechanisms observed at larger scales, although we are fully aware that the differences in system size and strain rate (which boosts twinning activity in the simulations) preclude a direct and quantitative comparison. However, our observations still confirm our initial hypothesis that the modeling results will provide scalable trends. While the structures in the FIB images in Fig. 2b and f are approximately two orders of magnitude larger, their qualitative agreement with the calculated micrographs in panels (c) and (e) shows that our simulations can reproduce the physics of the mechanisms because the system was constructed sufficiently large, i.e., featuring a mean grain size comfortably located within the Hall-Petch regime. We compared our microstructures to earlier MD work with grains in the 10 nm range,⁴¹ and differences were evident in the ability of the larger grains to accumulate and store dislocations within, while the smaller grains (10 nm and below) remained virtually dislocation-free because they are too small to store dislocations.

The white region in Fig. 2a lies below the normal pressure associated with the critical twinning stress $\tau_{\text{crit}}^{(\text{TB})}$ for that composition and marks the elastic regime. The green region is characterized by the onset of twinning and lattice rotation, as illustrated by the sections in panels (b–c). The FIB cross-section in panel (b), recorded in ion mode, reveals partial lattice rotation, visible as a smooth and gradual transition between gray-scale values, marked by a dashed white line. It should be noted that lattice rotation itself does not directly result in new grains, but that it can provide a distinct “environment” for them to grow,^{44,45} which is in good

qualitative agreement with the simulation in panel (c), despite the large difference in sliding speed between experiment (0.3 m/s) and simulation (80 m/s). Due to the high sliding speed, the latter also features strain rate induced twinning as shown on the right side of panel (c).

The yellow region lies above $\sigma_{\text{trans}}^{(\text{TB})}$, extracted from our simulations, which represents the resistance of an alloy to plastic deformation accompanied by grain refinement as well as increased twinning. Here we observe pronounced grain boundary dominated plastic deformation, both computationally and experimentally, see Fig. 2d–e. Both panels show the formation of new small grains via lattice rotation, and the simulated microstructure in panel (d) is accompanied by twin formation. The boundary between the green and the yellow regions is also in good agreement with the normal pressure associated with the onset of grain refinement in our simulations.

When entering the blue region coming from the yellow one, we find systems characterized by highly refined grains that are now subjected to massive twinning, see panel (f). With increasing normal pressure, this is accompanied by stress-induced grain growth^{20,46} as the mean shear layer thickness d_{shear} , which will be discussed in detail in the next section, exceeds a threshold value of 2 nm and can no longer be neglected. The value chosen for this threshold is motivated by the need to filter out any direct influence of the counterbody asperities (which at an RMS roughness of 0.5 nm lie within that depth range) on the identification of an emerging shear layer. The location of the curve dividing the yellow and the blue region coincides well with the normal pressure at which the slopes of the shear stress and the real contact area as functions of the normal pressure flatten abruptly (see Figs. S1 and S2 in the Supporting Information), indicating a transition in the dominating deformation mechanism. In our confined model system, the blue region can also be seen as a “transition

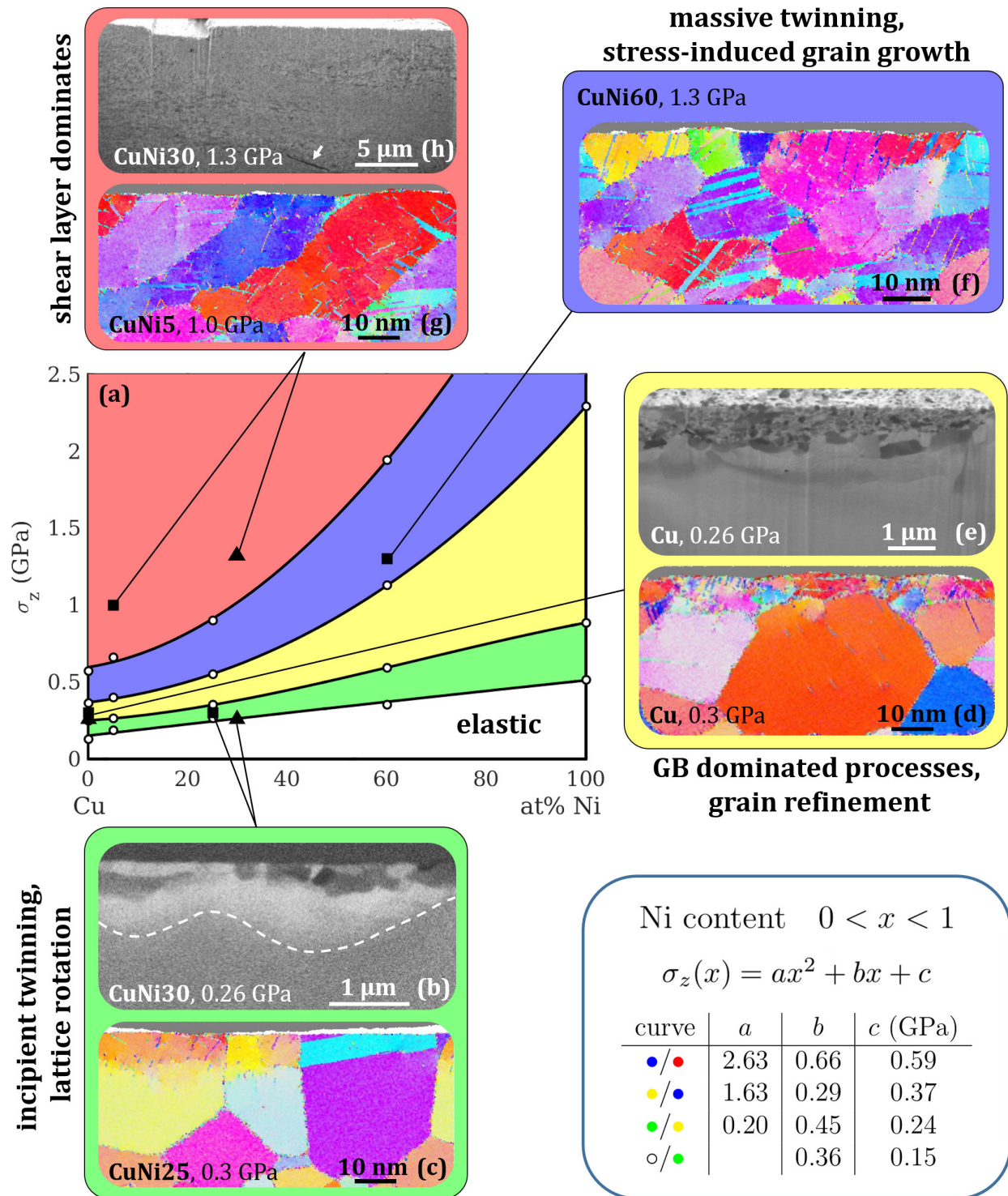


Figure 2: (a) The deformation mechanism map as a function of composition and normal contact pressure. White data points are derived from our MD simulation results, and regime boundaries are polynomial fits with the parameters listed in the lower right corner. (b–h) Representative computational and experimental microstructures; the panels are color-coded according to the regimes in the map. The dashed curve in (b) indicates the lower boundary of the region affected by lattice rotation.

regime” between locally (surface) and globally (sample) dominated behavior.

Finally, in the red region, the shear layer dominates the behavior of the entire system. Here the normal contact pressures exceed the value beyond which d_{shear} becomes larger than the thickness of the previously formed refined grains layer (d_{refined}). This region is characterized morphologically by large elongated grains, spanning almost the entire sample thickness in the simulation, see panel (g). This domain may be considerably influenced by the confinement of the model system, as will be discussed in the next section. From the existing data it is therefore not possible to confirm the exact values of the system-independent transition from the blue to the red region, as this is bound to depend on the size of the sample under investigation. In this context, the boundaries between the regions of the map corresponding to grain growth and shear layer domination are more likely to correspond to those that might be observed in soft metallic coatings deposited on hard substrates, where confinement effects play a major role.

The experimental FIB cut in panel (h) features a thick layer of small grains, which is accompanied by a wavy structure that was probably created by multiple folding events. The thin dark gray interface at the bottom right (marked by the arrow) is an indication for massive shear in the experimental setup, however occurring on a larger scale. Although the grain structure and size differences between panels (g) and (h) are obvious, the collective movement of a large number of grains, which can be observed in the videos in the Supporting Information and can be deduced from the folding structure and the folding interfaces, indicates similarities in material behavior during highly loaded sliding.

The fact that our simulations lead to grain refinement at lower pressures and ultimately to grain growth at high pressures agrees well with observations such as those in Ref. 20 regarding friction effects of microstructure in Au-based systems. The onset of plastic defor-

mation by partial grain rotation and refinement are equally reflected in the experiment and in the simulation. Just by looking at the map it becomes obvious that the alloy properties related to shear layer formation resistance improve rapidly even for small increases beyond 40% in the Ni content. Note that in our confined sliding MD system, no material is ever lost, therefore simulating wear in the classical sense is not explicitly possible. As anticipated above, any later stages observed at high pressures, such as shear layer formation and large elongated grains or the formation of interfaces by folding, are undesirable as large volumes moving collectively will most likely also wear off as one and presumably result in random wear events and unsteady friction.

Delving into the mechanisms

After having qualitatively described the dominant microstructural deformation mechanisms and introduced the deformation mechanism map we obtained from our simulations, we will now discuss the systematic approach to quantifying our observations in terms of grain refinement, atomic shear velocity, stresses in shear direction, and twinning. We first visualize the quantity of interest in the form of “heat maps” as a function of time and sample depth for every composition and load. The heat maps are further evaluated by identifying and justifying threshold values aimed at capturing the time evolution of sample regions, which are considered to be part of the “refined layer” and “shear layer”, or by integrating over the sample thickness to yield a total twin boundary fraction. We finally extract equilibrium values from the resulting time-dependent characteristics and present them as functions of load and composition.

It has been observed experimentally that tribological loading of copper leads to a well-defined boundary between a coarse and a refined region.⁴⁷ To explore this phenomenon in our simulated systems, we show an ex-

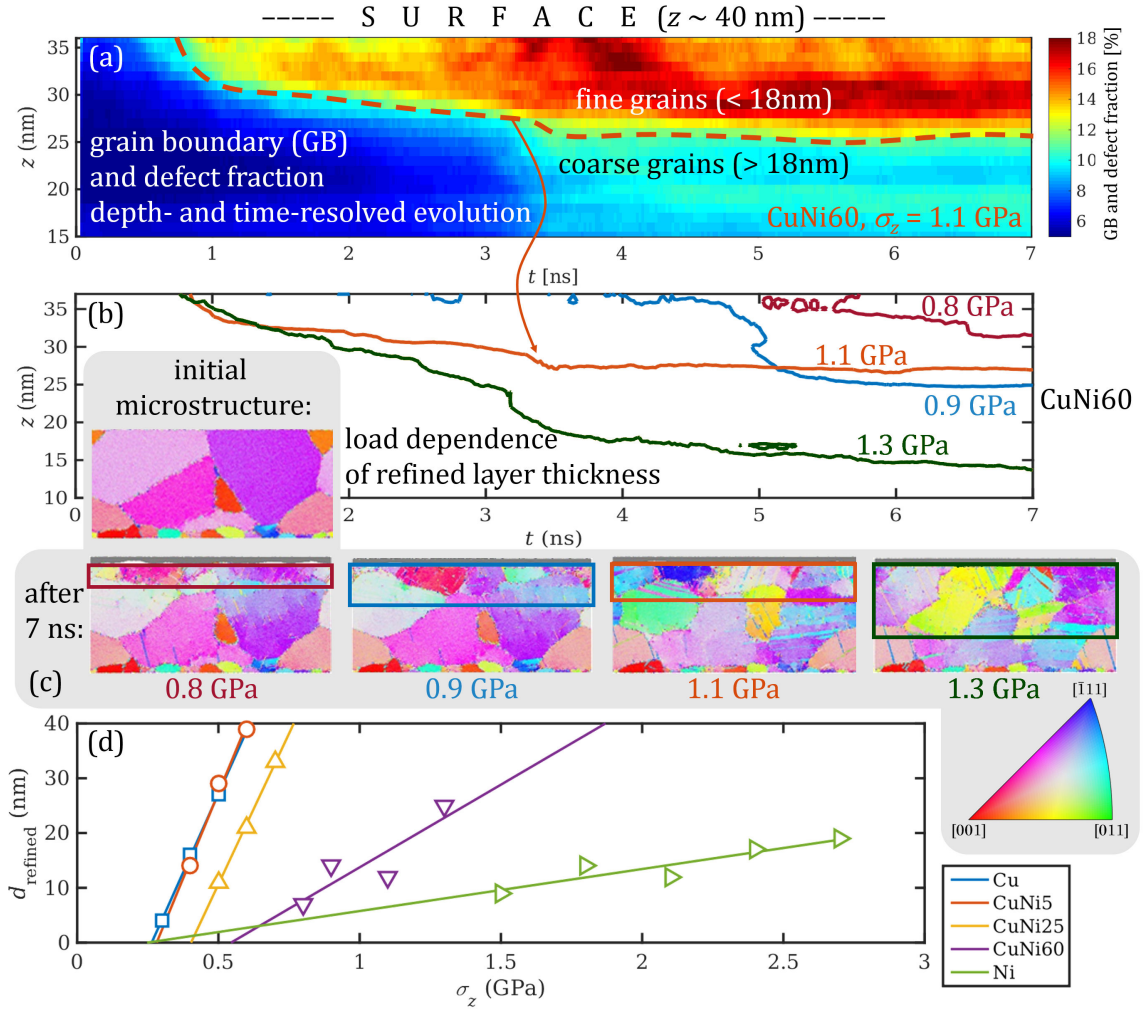


Figure 3: Grain refinement. The first three panels outline how the bottom panel is obtained for the example case of CuNi60. (a) Heat map visualizing the depth- and time-resolved evolution of the grain boundary and defect fraction for CuNi60 sliding at $\sigma_z = 1.1$ GPa. The dashed orange trace line separates the refined grains from the (original) coarse grains region. (b) All trace lines for CuNi60 at various applied loads are superimposed, and the equilibrium layer thickness d_{refined} is evaluated at $t = 7$ ns. (c) Representative tomographic sections for four normal pressures at $t = 7$ ns, with a colored box marking the refined grains region (compare with the initial microstructure at the top left). (d) The refined layer thickness d_{refined} is plotted as a function of normal pressure for all compositions. The lines are linear fits to the data.

emplary heat map in Fig. 3a, representing the depth- and time-resolved evolution of the grain boundary and defect fraction, henceforth referred to as GB fraction; this is obtained by summing up all non-FCC ordered atoms that are not part of a twin boundary. This quantity has been shown to be able to provide a measure for the grain size in FCC metals using a non-linear relationship.^{2,40} Corresponding heat maps for the other alloy compositions at several normal pressures can be found in the Supporting Information in Figs. S3–S6. The undeformed (40 nm) grains correspond to a GB fraction of approximately 5%, while the refined (10 nm) grains correspond to about 20%. Therefore, we parametrically varied the GB fraction threshold to identify the transition between a coarse and a refined grains region in the polycrystalline aggregate. In particular, we evaluated the contours resulting from analyzing the GB fraction range 10–14%, see Fig. S7 in the Supporting Information. The clearest distinction between the two regions could be made when setting the GB fraction threshold to 18 nm (or 11%), yielding a clearly evolving boundary line that divides the refined grains region, with grains smaller than 18 nm, from the bulk.

Plotting the iso-GB-fraction curves for a number of normal pressures of a given composition, as shown in Fig. 3b for CuNi60 (and in Fig. S8 in the Supporting Information for the other compositions), shows how the normal pressure influences the time evolution of the refined layer thickness. In general, the higher the contact pressure, the earlier the refined layer begins forming, and the deeper it extends into the polycrystalline aggregate. To illustrate this, the equilibrium value d_{refined} is superimposed as a colored box over some representative computational tomographs of CuNi60 after 7 ns of sliding in Fig. 3c. By aggregating the data points of all simulations where a stable equilibrium value of d_{refined} can be evaluated, the load dependence of the refined layer thickness can be fitted using a linear trend for all compositions, see Fig. 3d.

From a physical point of view, this linear trend may be explained by how the volume affected by high stresses, which in turn lead to recovery and refinement, increases linearly with the normal pressure. This is much along the lines of Archard’s reasoning why wear is eventually proportional to load,^{48,49} namely because the contact area is proportional to load in the absence of a change in deformation mechanism. This is indeed also the case in our simulations, as can be seen in the load dependence of the contact area (shown in Fig. S2 in the Supporting Information), where an abrupt change in the slope marks the load where the dominating deformation mechanism changes. It should be noted that the linearity of the load dependence of the refined layer thickness is only claimed within the deformation regime where grain refinement dominates (the yellow region in Fig. 2a), and to a limited extent where massive twinning occurs and the shear layer starts forming (blue region). The slopes of the fit lines remain nearly constant up to Ni contents of 25% and then decrease rapidly. The non-zero intercepts of the fitted trends with the σ_z axis translate into a minimum normal pressure required for the onset of grain refinement. Owing to the shallow slope of the trend for Ni and the fact that the lowest available data point in terms of pressure lies at $\sigma_z = 1.5$ GPa, the extrapolation of this particular σ_z -intercept has to be considered unreliable.

The evaluation of the GB fraction performed above allows a quantitative analysis of grain refinement. Analogously, a plot of the advection velocities of the atoms in the polycrystalline aggregate in the direction of sliding instantaneously reveals which regions participate in the microstructural changes by rotation/sliding, or phenomena such as shear localization.³² Eventually, given sufficient normal pressure, most of the atoms move collectively, and the velocities clearly show the formation of a shear layer as the sliding interface moves towards the lower boundary of the simulation box.

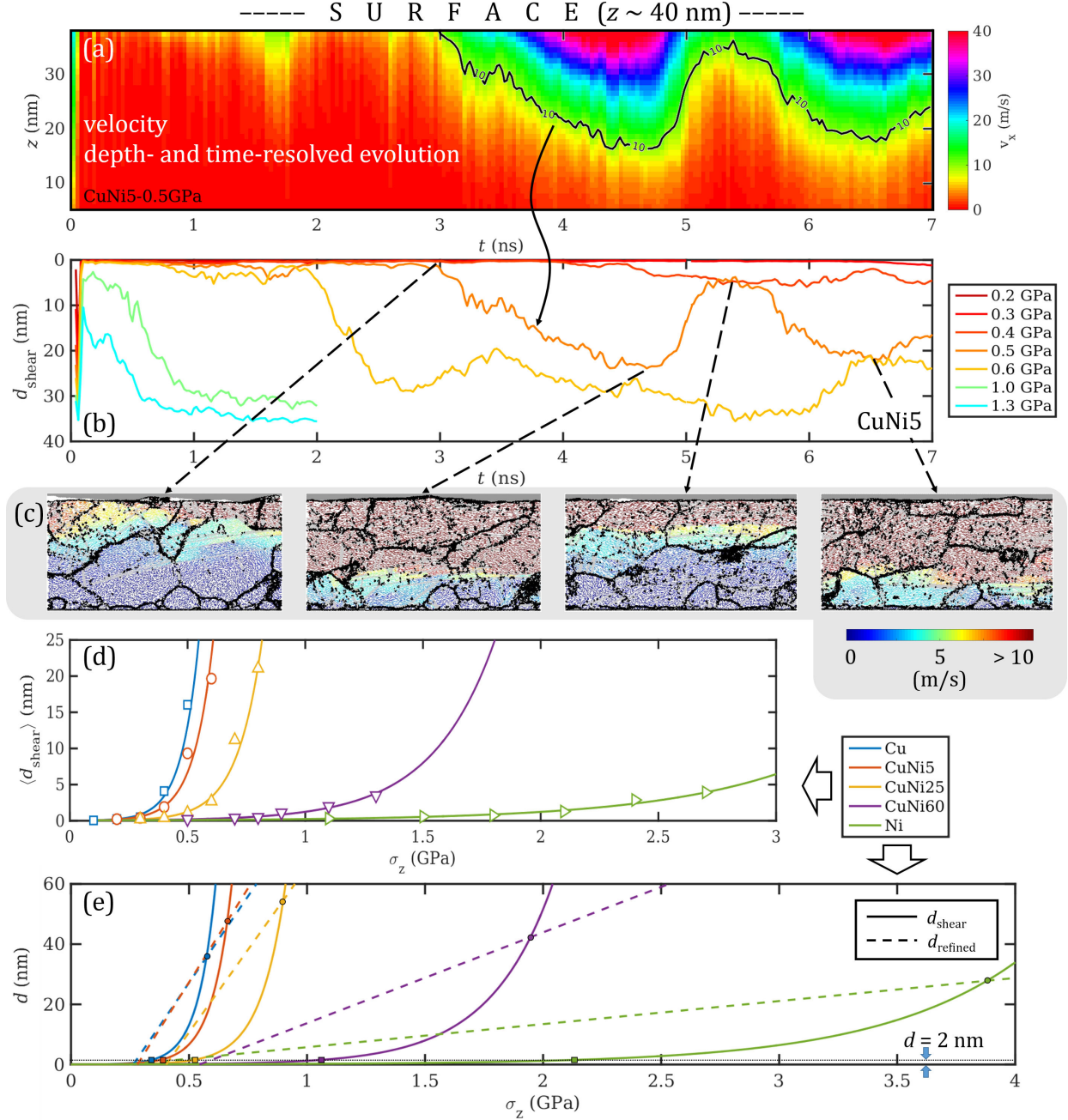


Figure 4: Formation of a shear layer. Example system: CuNi5. (a) Depth- and time-resolved evolution at 0.5 GPa of the atomic (advection) velocities, with a contour line at the threshold velocity of 10 m/s above which we consider the near-surface region under shear. (b) Time development of the shear layer thickness for several normal pressures. (c) Representative tomographic sections of CuNi5 at 0.5 GPa at the times indicated by the arrows. Jet-style coloring is according to advection velocity, see colorbar. Grain boundaries are black, twin boundaries gray. (d) Mean shear layer thickness d_{shear} over normal pressure for all compositions. (e) Intersection points (circles) of the trends for the shear layer thickness (solid lines) and the refined layer thickness (dashed lines). The intersection points with the threshold shear layer thickness of 2 nm (dotted line) are shown as squares.

An example of the depth- and time-resolved evolution of the atomic velocities in CuNi5 at 0.5 GPa is shown in Fig. 4a. Considering the sliding velocity of the counterbody of 80 m/s, the threshold differentiating between regions in the aggregate that are virtually at rest and those that are substantially sheared was set to 10 m/s. This threshold was chosen based on an evaluation of numerous velocity histograms, attempting to keep the value low and constant for all systems while de-emphasizing oscillations caused by small atomic displacements that are not associated with collective shear. The resulting iso-lines corresponding to the time development of the shear layer thickness d_{shear} are combined in Fig. 4b for all normal contact pressures that were considered for CuNi5. Analogous graphs for the other alloy compositions can be found in Fig. S9 in the Supporting Information. The time development of d_{shear} differs from that of d_{refined} in that it is not characterized by a monotonically increasing trend, i.e. a fully formed shear layer may potentially collapse and re-form. Evidently, shear layer formation is the result of a dynamic and at least partially reversible process. The tomographic slices in Fig. 4c are colored according to atomic velocity, where all atoms moving faster than the threshold velocity are shown in dark red, and illustrate the velocity distribution at selected times during the sliding process together with the grain boundaries at that state (shown in black).

Time-averaging the curves of d_{shear} and analyzing the logarithm of the mean values over the normal contact pressure suggests an exponential correlation between the two, see Fig. 4d or Fig. S10 in the Supporting Information for a semi-logarithmic plot. Initially, there is a strong resistance to form a shear layer, but increasing the stress brings the system closer to a fully-sliding condition due to the higher energy available within the boundaries of confinement. This means that the exponential response is similar to that of a solid that starts sliding and shifts from par-

tial to full slip; as the resistance to sliding is reduced, the force required to move further reaches a plateau. So the refined grains layer and the shear layer thicknesses feature fundamentally different dependencies on the contact pressure (linear *vs.* exponential): the former is intrinsically linked to the local area of influence of load, while the latter is rather a global resistance to move, which must have some form of saturation.

We can thus obtain the pressure ranges in which one or the other effect dominates by intersecting the fitted curves for each composition. The resulting intersection points, shown in Fig. 4e, define the contact pressures below which plasticity is dominated by grain refinement based on partial grain rotation followed by formation of smaller new grains. At higher contact pressures, these deformation mechanisms are increasingly replaced by grain boundary sliding, and eventually the shear layer dominates. Note that as most of the calculated intersection points lie in the extrapolated range of the fitted curves (compare with the data points in Fig. 4d), the resulting shear layer thickness may come out greater than the thickness of our model (40 nm). Thus, any conclusions drawn from the corresponding threshold contact pressures have to be seen in light of the limited model system size and may therefore be considerably influenced by confinement. However, the occurring trends provide valuable insight that may be transferred to more universal, size-independent statements. Once the shear layer dominates, further grain refinement would no longer be visible because of grain coalescence and growth, evidence of which has also been described based on experiments^{14,50} and mesoscale modelling.¹⁵ Eventually, the collectively moving grains form similarly oriented and comparatively large structures, which may be considered a result of grain coarsening at high contact stresses as discussed in.²⁰

In our third approach to analyzing the microstructural development, we combine information about the lateral stress distribu-

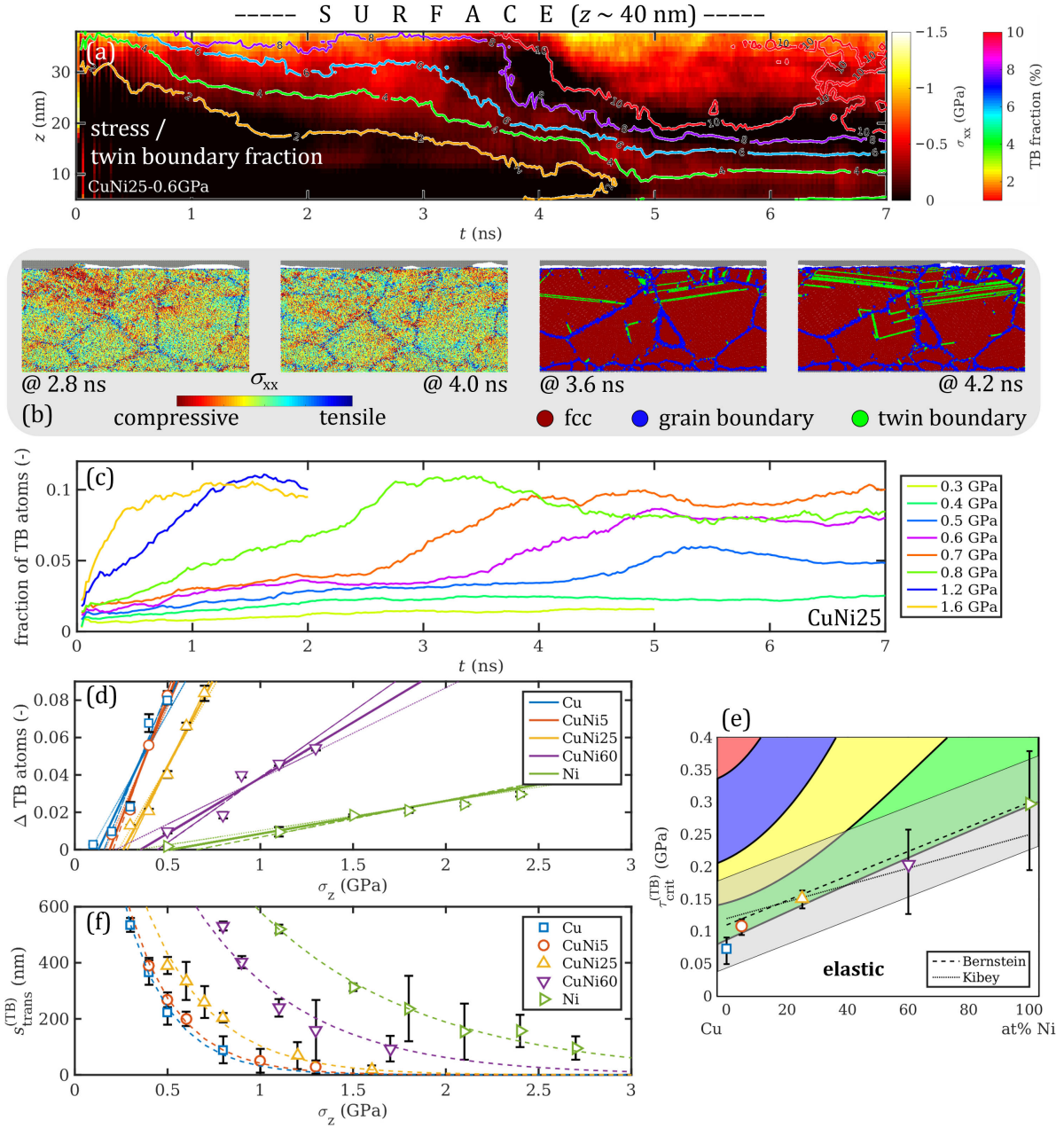


Figure 5: Development of stresses and twinning. Example system: CuNi25. (a) Depth- and time-resolved evolution at 0.6 GPa of the principal normal stress in sliding direction σ_{xx} (heat map) and the twin boundary (TB) fraction (contour plot). (b) representative tomographs to illustrate the near-surface stress release at $t \sim 3.2$ ns and the surge in TBs at $t \sim 4.0$ ns (c) Time development of the total TB fraction in CuNi25 at several normal pressures. (d) Δ TB (final minus minimum value) over normal pressure for all compositions. Lines are linear fits to the data. Dotted lines represent the uncertainty of the fits' slopes and axis intercepts due to the spread of the data. (e) Critical twinning stress over nickel content. Data points are from this work, error bars represent the ranges of the σ_z -axis intercepts marked by the dotted lines in panel d. The regimes from Fig. 2a are transferred for ease of comparison. (f) Mean sliding distance $s_{trans}^{(TB)}$ until sudden increase in TB fraction over normal pressure for all compositions. Error bars mark the beginning and the end of the step increase, and the dashed lines are exponential fits to the data.

tion σ_{xx} in the aggregate (heat map) with the twin boundary (TB) fraction distribution (iso-contours) in Fig. 5a. In the system CuNi, the SFE increases with the Ni content, and its value varies by approximately a factor of three between pure Cu and Ni. The TB fraction also includes stacking faults and Shockley partials, but to keep our nomenclature simple, we will refer to the quantity as the TB fraction henceforth (see Methods section for more details). The nucleation of twinning is mainly influenced by strain rate, temperature, and alloying.⁵¹ As temperature does not play an important role in FCC systems concerning the twinning stress, and due to our thermostatting scheme, no region in the aggregate heats up by more than some tens of K, we can neglect any thermal influence. In Fig. 5a, the sudden increase of the twin boundary fraction beyond 8% down to depths of approximately 20 nm, which is governed by twinning nucleation, is accompanied by a drop in the previously built up near-surface stress at $t \sim 3.5 - 4.5$ ns. The subsequent growth of the twins requires far less stress, which cannot be resolved in our simulations due to thermal noise. All systems that feature this sudden TB increase at a given normal contact pressure also exhibit the concurrent stress release, illustrated in the before/after tomographs in Fig. 5b (as well as in the heat maps at several normal pressures in Fig. S11 in the Supporting Information), from which it can also be seen that the stress field underneath the contact areas is strongly non-homogeneous. The sliding distance after which this rather sudden release of stress occurs depends on the load and the composition. Note that the stress visualized in Fig. 5a is averaged over the entire sample at a given depth. By contrast, the tomographs in Fig. 5b show a spatially resolved stress distribution at a selected vertical cross-section, clearly revealing the lateral accumulation of stress in certain grains. This accumulation is followed by recovery as the microstructure changes either by forming more twin boundaries or by further grain rotation. Since the

stress release and the twin boundary increase occur simultaneously, one might be led to believe that the former is caused by the latter. However, the two are not as directly and simply connected due to the localized adaptation of the microstructure to reduce stresses, even in our comparatively small system. Yet, at sufficiently high pressures eventually the stress cannot be released any more, at which point the substrate begins transforming into a shear layer completely, cf. the discussion of Fig. 4. Once the stress reaches a saturation level, the entire substrate behaves similar to a fluid due to nearly perfect gliding as an aggregate, where the Couette-like flow within the shear layer ends abruptly at the transition to the rigid monolayers at the lower boundary of the system; this is something often observed in confinement and layered systems, where phase transformations and shearing mechanisms are controlled by local ordering and thermodynamic conditions as well as the geometric constraints imposed on the sheared material.^{14,36,43,52} At higher normal contact pressures, where the stress release occurs earlier, we see evidence of a reduction in twin boundaries while the stress begins to build up again.

By integrating the TB fraction distribution over the sample depth, we obtain the total TB fraction over time, shown for CuNi25 in Fig. 5c and for all alloy compositions in Fig. S12 in the Supporting Information. The resulting trend curves qualitatively reflect the more complex heat maps very well and all feature a period where the TB fraction rises more sharply than elsewhere. As a general rule, the higher the normal contact pressure, the larger the difference ΔTB between the minimum and the final TB fraction, as shown for all compositions in Fig. 5d. Here, we observe that twinning is eventually hindered by the larger SFE for Ni rich alloys. The thick lines are linear fits to the data, and the pairs of dotted lines represent the margin of fitting error according to the spread of the data. An extrapolation of the obtained trends to $\Delta\text{TB} = 0$ yields the normal pressure above

which twinning begins to occur for a given composition, where the intercepts of the dotted lines provide an error estimation. The results were incorporated into the deformation mechanism map as the separation curve between the white and the green region, and they allow the deduction of the critical twinning stress $\tau_{crit}^{(TB)}$ as a function of composition by dividing the obtained σ_z -axis intercepts by $\sqrt{3}$. This follows from a straightforward argument based on the von Mises plasticity law and the link between yield stress in pure shear and under uniaxial loading.⁵³ Our own $\tau_{crit}^{(TB)}$ values are shown as data points with error bars depending on the composition in Fig. 5e. We compare our results with data from Refs.,^{54,55} and the gray band marks the uncertainty of the literature values for Cu (from⁵⁴), extended to all alloy systems accordingly.

Furthermore, the higher the pressure, the shorter the mean sliding distance $s_{trans}^{(TB)}$ at which the sudden increase in the TB fraction occurs. This behavior is plotted against the normal contact pressure in Fig. 5f, where the error bars mark the beginning and the end of the steep increase. The dashed curves are fits to the function $s_0 \exp(-\sigma_z/\sigma_{trans}^{(TB)})$, where s_0 is a composition-independent constant of approximately 1800 nm. This can be interpreted as a “typical grain boundary length”, which is a function of geometric conditions such as the system size and the mean grain size, but not of the composition. To justify this, we can project the initial grain boundary fraction of $5 \pm 0.75\%$ onto the surface, yielding $360 \pm 55 \text{ nm}^2$. Dividing this value by a minimum grain boundary width of 0.253 nm (a mean interatomic first-neighbor distance for CuNi systems), we obtain $1425 \pm 220 \text{ nm}$ of grain boundary length for our system and grain size. This quantity potentially provides a way to quantify the likelihood of a specific microstructure to develop TB under sliding when subjected to a certain applied pressure: the smaller it is, the less likely for TB to develop for a given external load.

The parameter $\sigma_{trans}^{(TB)}$ has the dimension of a stress and depends on the composition. Cu has the lowest $\sigma_{trans}^{(TB)}$ value, 240 MPa, and the values rise monotonically with increasing Ni content up to 890 MPa, a relative increase that is comparable with that of the SFE. Thus, $\sigma_{trans}^{(TB)}$ may be interpreted as a characteristic stress value for a material or alloy composition that determines the resistance to plastic deformation by twinning. This is in good agreement with the dependence on SFE and the twinning tendency as proposed by Asaro *et al.*, where Cu shows a stronger tendency towards twinning than Ni.⁵⁶ As the total GB fraction features a time development similar to that of the TB fraction in terms of its gradient (shown in Fig. S13), $\sigma_{trans}^{(TB)}$ is also closely related to the resistance to forming new grains by lattice rotation.

It should finally be emphasized here that the presented method may not yet be predictive of *macroscale* behavior in a generalized way. Given the significant differences and constraints for parameters like grain size, shear rate, and surface roughness, as well as the importance of these to the strengths of macroscale contacts and the determination of a prevailing deformation mechanism, further work is needed to demonstrate and explain how this information can be translated into practical use, such as the prediction of the microstructure evolving in sliding FCC alloy contacts. Nonetheless, our work constitutes the necessary basis and provides the initial milestone to enable the evolution of the proposed methodology into an engineering tool for alloy surface design.

Conclusion

In this work we have demonstrated that large-scale MD simulations can produce compelling data that can be distilled into a deformation mechanism map for CuNi alloys, suggesting highly useful links that exist between simulations and macroscale experiments. By exploring and quantifying the phenomena of grain

refinement, twinning, stress build-up and release, as well as shear layer formation, we derived several characteristic contact pressures for each alloy that demarcate different deformation mechanism domains. Our model system clearly showed how alloying and thus varying the stacking fault energy can lead to different microstructural responses under sliding. This is reasonable, since the SFE as a fundamental material parameter significantly affects the twinning tendency of a material system, with an immediate impact on dislocation mobility. A high SFE leads to a reduced twinning tendency and thus to other accommodation channels for plastic deformation, which is well reproduced in our calculation results. We can therefore assume that our MD simulations can capture the relevant acting mechanisms so that the deformation mechanism map, while derived for the example of CuNi, is suitable to be applied to other FCC alloy systems as well.

Methods

Computational

All simulations were carried out using the open-source MD code LAMMPS.⁵⁷ The setup of the polycrystalline MD model of $85 \times 85 \times 40 \text{ nm}^3$, or approximately 25 million atoms, is explained in detail in.^{40,58} To maximize the degrees of freedom of the surface grains with an average diameter of $\sim 40 \text{ nm}$, a layer of $\sim 10 \text{ nm}$ grains was grafted to the sample bottom, to which the boundary constraints could be applied. Interactions within the FCC CuNi_x samples are controlled by an EAM potential from.³⁵ All alloy systems were heat treated at 650 K for 240 ps, after which they were quenched within 20 ps to 300 K. For the pure Ni system, the heat treatment temperature was 1050 K, and cooling to 300 K was slowed down to 200 ps. So while the initial model is based on a Voronoi construction where only some 12 grains make up more than 90% of the system, this heat

treatment ascertains that the triple junctions can equilibrate sufficiently. The counterbody is a bcc Fe(100) monocrystal with a Gaussian RMS surface roughness of 0.5 nm, a fractal dimension of 2.186, and a characteristic lateral asperity extent of 33 nm. It was kept several monolayers thin and rigid in order to maximize the computational resources for the simulation of the microstructural evolution of the sample, thus allowing us to treat grain sizes of 40 nm, but implying that the counterbody is considerably harder than the sample. Its modest roughness effectively ascertains a “no slip” interface condition between the two surfaces. For the interactions between the counterbody and the sample, Lennard-Jones potentials were adopted to imply a third body, so that the results reflect a typical sliding process that explicitly considers friction, rather than a sheared interface between two pure metal surfaces in ultra-high vacuum. Earlier work⁵⁹ refers to a parameter study that varied the adhesion between the interacting surfaces from scenarios with virtually no interaction to those with purely adhesion-dominated processes and immediate fully conformal contact. The narrow window between these two types of sliding system behavior led to our choice of a global energy parameter of $\epsilon = 0.095 \text{ eV}$, yielding an interaction roughly 25% weaker than that assumed in previous abrasion simulations.⁶⁰ The element-specific zero-intercepts $\sigma_{\text{Fe-Cu}} = 0.224 \text{ nm}$ and $\sigma_{\text{Fe-Ni}} = 0.221 \text{ nm}$ were calculated from interatomic first-neighbor distances using the Lorentz-Berthelot mixing rules.

The counterbody was moved across the surface of the sample at a sliding velocity in x direction of $v^{(\text{slide})} = 80 \text{ m/s}$ and an angle of 6.42° with the x -axis, so that roughness features re-enter the simulation box at different y positions every time they pass the periodic box boundaries and therefore never follow exactly in their own paths, which reduces artifacts associated with the small system size. The initial pairing of features on the base body and the counterbody is thus reached

again after sliding for approximately 750 nm. The normal pressure σ_z on the substrate was kept constant at values ranging from 0.2 to 0.8 GPa for pure Cu, 0.2 to 1.3 GPa for CuNi5, 0.3 to 1.6 GPa for CuNi25, 0.5 to 1.7 GPa for CuNi60, and 0.5 to 2.7 GPa for pure Ni for simulation times of 2, 5, or 7 ns, depending on what the data was used for.

A Langevin thermostat with a time constant of 0.5 ps acted on all the non-rigid base body atoms to remove the heat produced during sliding. This is equivalent to an electron-phonon coupling scheme where the electrons act as an implicit heat bath to mimic the electronic contribution to the thermal conductivity in a metal.⁴¹ The thermostat acts only in y direction, (nearly) perpendicular to the directions of sliding and normal pressure in order not to interfere with these external constraints.

Tomographic xz -sections colored according to the grain orientations (EBSD-IPF standard) were calculated in OVITO⁶¹ using polyhedral template matching,⁶² and the projection of the resulting quaternions into the EBSD-IPF color space was done with the MTEX toolbox⁶³ for Matlab.

Grain refinement and twinning were quantified via common neighbor analysis (CNA)⁶⁴ with a neighborhood cutoff radius of 0.3086 nm for all systems containing Cu, and 0.3005 nm for pure Ni. It should be noted that CNA cannot distinguish between grain boundaries, defects, and surfaces, as well as between twin boundaries, stacking faults, and Shockley partials. We have attempted to remove as much ambiguity as possible, e.g., by not showing any data too close to the sample surface, but have chosen to keep our nomenclature simple by referring only to grain boundary (GB) and twin boundary (TB) atoms. Histograms of the identified GB and TB atoms along the z direction of the samples with a bin width of 1 nm were normalized to GB and TB fractions at every time step to yield the depth- and time-dependent evolution of these quantities.

To show the formation of the near-surface shear layer, tomographic vector plots of the atomic advection velocities were produced (more details on the evaluation can be found in 65). By calculating the distance between the positions of an atom at two time steps that are 40 ps apart and associating the obtained average velocity with the atomic position exactly between these two time steps, thermal fluctuations are effectively eliminated, much in the fashion of a low-pass filter. In this way, the thickness of the shear layer may be quantified via the assumption of a threshold velocity that must be small (in our case 10 m/s) compared to the sliding speed of 80 m/s. However, this view of the system also allows a qualitative assessment of this layer as well as statements about slower processes within the polycrystalline aggregate that affect the microstructural development.

Heat maps representing the depth- and time-dependent evolution of the stress tensor component σ_{xx} were produced based on an on-the-fly evaluation, assuming a constant average per-atom volume within a 1 nm thick slab containing approximately 600k atoms. This approach also mitigates the issue of LAMMPS actually producing stress output in a stress \times volume formulation, where an atomic volume is not easily defined. By dividing the stress \times volume output value averaged over a 1 nm slab by the entire slab volume, the influence of the individual atoms' volumetric fluctuations is effectively suppressed. Averaging over so many atoms produces enough detail in the maps without the necessity for an energy minimization at every time step. Minimization was only carried out for the production of a few exemplary tomographic stress distribution sections of selected compositions/pressures/times.

The curves separating the different regimes in the deformation mechanism map are first- and second-order polynomials fitted to the white data points in Fig. 2a, and their parameters are listed in Table ?? so that the

map may be easily reconstructed for practical application.

Experimental

The experimental verification was done on flat plate samples made of technically pure Cu (obtained by repeated electrolytic refinement leading to a typical purity of 99.90–99.95wt% with a strongly reduced oxygen content), a binary alloy with 30wt% Ni, and pure Ni with a purity of 99.9wt%. The samples were all ground on SiC paper till #500, followed by polishing with 9 μm and 3 μm diamond particles, then high-gloss polished with 0.25 μm . Finally, the pure Ni and the CuNi30 samples were chemically polished with aluminum oxide (Struers OP-AA) and thoroughly rinsed with water to remove all abrasives and polishing liquids.

The plate samples were placed in an SRV device from Optimol, and a 100Cr6 ball with 20 mm diameter was used to slide in a dry contact oscillating over 3 mm stroke till a sliding distance of 3 m was reached. The tests were performed at various normal loads resulting in different Hertzian pressures ranging from 470 MPa (max. Hertzian Pressure) for Cu to 890 MPa for Cu and 610 MPa to 1140 MPa for Ni. CuNi30 was loaded at 550 MPa, 960 MPa, and 1300 MPa. The aim was to perform the sliding experiments at different pressure levels that cover the simulated regimes. The reason for the varying applied pressure values originates in consistent normal loads, but the variation of Young’s modulus for the different alloys.

After the sliding test the samples were analyzed using a focused ion beam (FIB) cross-section perpendicular to the sliding direction in the middle of the wear track, where the sliding velocity reaches its maximum. The FIB cut and the following grain structure analysis were performed on a HRSEM with a field emission electron source (Zeiss SUPRA VP40), equipped with a Ga²⁺ ion beam gun. Typically, FIB cuts of a length of 30 μm and

a depth of 10 μm were cut to analyze the microstructure beneath the wear track. Portions of the grains further away from the surface were cropped if they provided no additional information.

Acknowledgements

This work was funded by the Austrian COMET-Program (Project K2, XTribology, no. 849109, and InTribology1, no. 872176) and carried out at the “Excellence Centre of Tribology”. The government of Lower Austria is gratefully acknowledged for financially supporting the endowed professorship tribology at the TU Wien (Grant no. WST3-F-5031370/001-2017) in collaboration with AC2T research GmbH. D.D. acknowledges the support of the Engineering and Physical Sciences Research Council (EP-SRC) via his Established Career Fellowship EP/N025954/1. The computational results presented have been achieved in part using the Vienna Scientific Cluster (VSC). The authors would like to thank Ashlie Martini and Christian Greiner for reading through the manuscript and making many important suggestions.

Supporting Information

Fig. S1: Global shear stress over normal pressure for Cu, CuNi5, CuNi25, CuNi60, and Ni.

Fig. S2: Relative contact area over normal pressure for CuNi5, CuNi25, CuNi60, and Ni.

Fig. S3: Heat maps of the grain boundary fraction for CuNi5.

Fig. S4: Heat maps of the grain boundary fraction for CuNi25.

Fig. S5: Heat maps of the grain boundary fraction for CuNi60.

Fig. S6: Heat maps of the grain boundary fraction for Ni.

Fig. S7: On the determination of the best grain boundary fraction threshold value for

differentiating between the bulk and the refined grains layer.

Fig. S8: Formation of the refined grains layer for CuNi5, CuNi25, CuNi60, and Ni.

Fig. S9: Development of the shear layer thickness for CuNi5, CuNi25, CuNi60, and Ni.

Fig. S10: Semilogarithmic plot of the mean shear layer thickness over normal pressure.

Fig. S11: Principal normal stress in sliding direction (heat map) and twin boundary fraction (contour plot) depth profile and time development for CuNi25.

Fig. S12: Time development of the total twin boundary fraction in CuNi5, CuNi25, CuNi60, and Ni.

Fig. S13: Time development of the total grain boundary fraction in CuNi5, CuNi25, CuNi60, and Ni.

Video 1: Sliding of CuNi25 at 0.8 GPa colored according to grain orientation (EBSD).

Video 2: Sliding of CuNi25 at 0.8 GPa colored according to advection velocity.

References

- (1) Greiner, C.; Gagel, J.; Gumbsch, P. Solids Under Extreme Shear: Friction-Mediated Subsurface Structural Transformations. *Advanced Materials* **2019**, *31*, 1806705.
- (2) Li, A.; Szlufarska, I. How grain size controls friction and wear in nanocrystalline metals. *Physical Review B* **2015**, *92*, 075418.
- (3) Lu, K.; Lu, L.; Suresh, S. Strengthening materials by engineering coherent internal boundaries at the nanoscale. *Science* **2009**, *324*, 349–352.
- (4) Hughes, D.; Hansen, N. Graded nanostructures produced by sliding and exhibiting universal behavior. *Physical Review Letters* **2001**, *87*, 135503.
- (5) Meyers, M. A.; Mishra, A.; Benson, D. J. Mechanical properties of nanocrystalline materials. *Progress in materials science* **2006**, *51*, 427–556.
- (6) Schiøtz, J.; Jacobsen, K. W. A maximum in the strength of nanocrystalline copper. *Science* **2003**, *301*, 1357–1359.
- (7) Karthikeyan, S.; Agrawal, A.; Rigney, D. Molecular dynamics simulations of sliding in an Fe–Cu tribopair system. *Wear* **2009**, *267*, 1166–1176.
- (8) Milanese, E.; Brink, T.; Aghababaei, R.; Molinari, J.-F. Emergence of self-affine surfaces during adhesive wear. *Nature communications* **2019**, *10*, 1116.
- (9) Kuo, S.; Rigney, D. Sliding behavior of aluminum. *Materials Science and Engineering: A* **1992**, *157*, 131–143.
- (10) Chen, X.; Han, Z.; Lu, K. Wear mechanism transition dominated by subsurface recrystallization structure in Cu–Al alloys. *Wear* **2014**, *320*, 41–50.
- (11) Greiner, C.; Liu, Z.; Schneider, R.; Pastewka, L.; Gumbsch, P. The origin of surface microstructure evolution in sliding friction. *Scripta Materialia* **2018**, *153*, 63–67.
- (12) Chen, X.; Schneider, R.; Gumbsch, P.; Greiner, C. Microstructure evolution and deformation mechanisms during high rate and cryogenic sliding of copper. *Acta Materialia* **2018**, *161*, 138–149.
- (13) Karthikeyan, S.; Wu, J.-H.; Rigney, D. A. The role of vorticity in the formation of tribomaterial during sliding. *MRS Online Proceedings Library Archive* **2004**, *821*, 9.6.1.
- (14) Luo, Z.-P.; Zhang, G.-P.; Schwaiger, R. Microstructural vortex formation during cyclic sliding of Cu/Au multilayers. *Scripta Materialia* **2015**, *107*, 67–70.

- (15) Pouryazdan, M.; Kaus, B. J.; Rack, A.; Ershov, A.; Hahn, H. Mixing instabilities during shearing of metals. *Nature communications* **2017**, *8*, 1611.
- (16) Argibay, N.; Furnish, T.; Boyce, B.; Clark, B.; Chandross, M. Stress-dependent grain size evolution of nanocrystalline Ni-W and its impact on friction behavior. *Scripta Materialia* **2016**, *123*, 26–29.
- (17) Rupert, T. J.; Schuh, C. A. Sliding wear of nanocrystalline Ni-W: Structural evolution and the apparent breakdown of Archard scaling. *Acta Materialia* **2010**, *58*, 4137–4148.
- (18) Hughes, D.; Hansen, N. Exploring the limit of dislocation based plasticity in nanostructured metals. *Physical review letters* **2014**, *112*, 135504.
- (19) Prasad, S. V.; Battaile, C. C.; Kotula, P. G. Friction transitions in nanocrystalline nickel. *Scripta Materialia* **2011**, *64*, 729–732.
- (20) Argibay, N.; Chandross, M.; Cheng, S.; Michael, J. R. Linking microstructural evolution and macro-scale friction behavior in metals. *Journal of Materials Science* **2017**, *52*, 2780–2799.
- (21) Warner, D.; Curtin, W.; Qu, S. Rate dependence of crack-tip processes predicts twinning trends in fcc metals. *Nature materials* **2007**, *6*, 876.
- (22) An, X.; Wu, S.; Wang, Z.; Zhang, Z. Significance of stacking fault energy in bulk nanostructured materials: Insights from Cu and its binary alloys as model systems. *Progress in Materials Science* **2019**,
- (23) Moshkovich, A.; Lapsker, I.; Feldman, Y.; Rapoport, L. Severe plastic deformation of four FCC metals during friction under lubricated conditions. *Wear* **2017**, *386*, 49–57.
- (24) Wert, J.; Singerman, S.; Caldwell, S.; Quarles, R. The role of stacking fault energy and induced residual stresses on the sliding wear of aluminum bronze. *Wear* **1983**, *91*, 253–267.
- (25) Feller, H.; Gao, B. Correlation of tribological and metal physics data: the role of stacking fault energy. *Wear* **1989**, *132*, 1–7.
- (26) Suh, N.; Saka, N. The stacking fault energy and delamination wear of single-phase fcc metals. *Wear* **1977**, *44*, 135–143.
- (27) Yamakov, V.; Wolf, D.; Phillpot, S.; Mukherjee, A.; Gleiter, H. Deformation-mechanism map for nanocrystalline metals by molecular-dynamics simulation. *Nature materials* **2004**, *3*, 43–47.
- (28) Verschueren, J.; Gurrutxaga-Lerma, B.; Balint, D.; Sutton, A.; Dini, D. Instabilities of high speed dislocations. *Physical review letters* **2018**, *121*, 145502.
- (29) Powell, C. A.; Michels, H. T. Copper-nickel alloys for seawater corrosion resistance and anti-fouling: a state of the art review. *CORROSION* 2000. 2000.
- (30) Noguchi, M. Sliding member, rotary device, and method for manufacturing sliding member. 2019; US Patent 10,505,328.
- (31) Stoyanov, P.; Harrington, K. M.; Frye, A. Insights into the Tribological Characteristic of Cu-Based Coatings Under Extreme Contact Conditions. *JOM* **2020**, 1–7.
- (32) Romero, P. A.; Järvi, T. T.; Beckmann, N.; Mrovec, M.; Moseler, M. Coarse graining and localized plasticity between sliding nanocrystalline metals. *Physical review letters* **2014**, *113*, 036101.

- (33) Dmitriev, A. I.; Nikonov, A. Y.; Österle, W. Molecular dynamics sliding simulations of amorphous Ni, Ni-P and nanocrystalline Ni films. *Computational Materials Science* **2017**, *129*, 231–238.
- (34) Pan, Z.; Rupert, T. J. Mechanisms of near-surface structural evolution in nanocrystalline materials during sliding contact. *Physical Review Materials* **2017**, *1*, 043602.
- (35) Bonny, G.; Pasianot, R. C.; Castin, N.; Malerba, L. Ternary Fe–Cu–Ni many-body potential to model reactor pressure vessel steels: first validation by simulated thermal annealing. *Philosophical magazine* **2009**, *89*, 3531–3546.
- (36) Beckmann, N.; Romero, P. A.; Linsler, D.; Dienwiebel, M.; Stolz, U.; Moseler, M.; Gumbsch, P. Origins of Folding Instabilities on Polycrystalline Metal Surfaces. *Phys. Rev. Applied* **2014**, *2*, 064004.
- (37) Karthikeyan, S.; Kim, H.; Rigney, D. Velocity and strain-rate profiles in materials subjected to unlubricated sliding. *Physical review letters* **2005**, *95*, 106001.
- (38) Zhao, M.; Li, J.; Jiang, Q. Hall–Petch relationship in nanometer size range. *Journal of alloys and compounds* **2003**, *361*, 160–164.
- (39) Van Swygenhoven, H. Grain boundaries and dislocations. *Science* **2002**, *296*, 66–67.
- (40) Eder, S. J.; Cihak-Bayr, U.; Gachot, C.; Rodríguez Ripoll, M. Interfacial Microstructure Evolution due to Strain Path Changes in Sliding Contacts. *ACS Applied Materials & Interfaces* **2018**, *10*, 24288–24301.
- (41) Eder, S. J.; Cihak-Bayr, U.; Bianchi, D.; Feldbauer, G.; Betz, G. Thermostat Influence on the Structural Development and Material Removal during Abrasion of Nanocrystalline Ferrite. *ACS Applied Materials & Interfaces* **2017**, *9*, 13713–13725.
- (42) Frank, C. Orientation Mapping: 1987 MRS Fall Meeting Von Hippel Award Lecture. *MRS Bulletin* **1988**, *13*, 24–31.
- (43) Ewen, J. P.; Gattinoni, C.; Zhang, J.; Heyes, D. M.; Spikes, H. A.; Dini, D. On the effect of confined fluid molecular structure on nonequilibrium phase behaviour and friction. *Physical Chemistry Chemical Physics* **2017**, *19*, 17883–17894.
- (44) Sebald, R.; Gottstein, G. Modeling of recrystallization textures: interaction of nucleation and growth. *Acta materialia* **2002**, *50*, 1587–1598.
- (45) Dorner, D.; Adachi, Y.; Tsuzaki, K. Periodic crystal lattice rotation in microband groups in a bcc metal. *Scripta Materialia* **2007**, *57*, 775–778.
- (46) Lin, Y.; Wen, H.; Li, Y.; Wen, B.; Liu, W.; Lavernia, E. J. An analytical model for stress-induced grain growth in the presence of both second-phase particles and solute segregation at grain boundaries. *Acta Materialia* **2015**, *82*, 304–315.
- (47) Greiner, C.; Liu, Z.; Strassberger, L.; Gumbsch, P. Sequence of stages in the microstructure evolution in copper under mild reciprocating tribological loading. *ACS Applied Materials & Interfaces* **2016**, *8*, 15809–15819.
- (48) Archard, J.; Hirst, W. The wear of metals under unlubricated conditions. *Proceedings of the Royal Society of London. Series A. Mathematical and Physical Sciences* **1956**, *236*, 397–410.
- (49) Villaggio, P. Wear of an elastic block. *Meccanica* **2001**, *36*, 243–250.

- (50) Sagapuram, D.; Viswanathan, K.; Trumble, K. P.; Chandrasekar, S. A common mechanism for evolution of single shear bands in large-strain deformation of metals. *Philosophical Magazine* **2018**, *98*, 3267–3299.
- (51) Meyers, M.; Vöhringer, O.; Lubarda, V. The onset of twinning in metals: a constitutive description. *Acta materialia* **2001**, *49*, 4025–4039.
- (52) Gattinoni, C.; Heyes, D. M.; Lorenz, C. D.; Dini, D. Traction and nonequilibrium phase behavior of confined sheared liquids at high pressure. *Physical Review E* **2013**, *88*, 052406.
- (53) Hill, R. *The mathematical theory of plasticity*; Oxford university press, 1998; Vol. 11.
- (54) Bernstein, N.; Tadmor, E. Tight-binding calculations of stacking energies and twinnability in fcc metals. *Physical Review B* **2004**, *69*, 094116.
- (55) Kibey, S.; Liu, J.; Johnson, D.; Sehitoglu, H. Predicting twinning stress in fcc metals: Linking twin-energy pathways to twin nucleation. *Acta Materialia* **2007**, *55*, 6843–6851.
- (56) Asaro, R. J.; Suresh, S. Mechanistic models for the activation volume and rate sensitivity in metals with nanocrystalline grains and nano-scale twins. *Acta Materialia* **2005**, *53*, 3369–3382.
- (57) Plimpton, S. J. Fast parallel algorithms for short-range molecular dynamics. *J. Comput. Phys.* **1995**, *117*, 1–19.
- (58) Eder, S. J.; Bianchi, D.; Cihak-Bayr, U.; Gkagkas, K. Methods for atomistic abrasion simulations of laterally periodic polycrystalline substrates with fractal surfaces. *Comput. Phys. Commun.* **2017**, *212*, 100–112.
- (59) Eder, S. J.; Cihak-Bayr, U.; Vernes, A.; Betz, G. Evolution of topography and material removal during nanoscale grinding. *Journal of Physics D: Applied Physics* **2015**, *48*, 465308.
- (60) Eder, S. J.; Cihak-Bayr, U.; Bianchi, D. Single-asperity contributions to multi-asperity wear simulated with molecular dynamics. *IOP Conference Series: Materials Science and Engineering* **2016**, *119*, 012009.
- (61) Stukowski, A. Visualization and analysis of atomistic simulation data with OVITO—the Open Visualization Tool. *Modelling and Simulation in Materials Science and Engineering* **2009**, *18*, 015012.
- (62) Larsen, P. M.; Schmidt, S.; Schiøtz, J. Robust structural identification via polyhedral template matching. *Modelling and Simulation in Materials Science and Engineering* **2016**, *24*, 055007.
- (63) Bachmann, F.; Hielscher, R.; Schaeben, H. Texture analysis with MTEX—free and open source software toolbox. *Solid State Phenomena*. 2010; pp 63–68.
- (64) Tsuzuki, H.; Branicio, P. S.; Rino, J. P. Structural characterization of deformed crystals by analysis of common atomic neighborhood. *Computer physics communications* **2007**, *177*, 518–523.
- (65) Eder, S. J.; Cihak-Bayr, U.; Bianchi, D. Large-scale molecular dynamics simulations of nanomachining. *Advanced Machining Processes: Innovative Modeling Techniques* **2017**, 141.